ARTICLE OPEN

Check for updates

Hong-Ou-Mandel interference of single-photon-level pulses stored in independent room-temperature quantum memories

Sonali Gera[1,5], Chase Wallace[1,5], Mael Flament[2], Alessia Scriminich[3], Mehdi Namazi[2], Youngshin Kim[1], Steven Sagona-Stophel[1], Giuseppe Vallone[3], Paolo Villoresi[3] and Eden Figueroa[1,4]✉

Quantum repeater networks require independent absorptive quantum memories capable of storing and retrieving indistinguishable photons to perform high-repetition entanglement swapping operations. The ability to perform these coherent operations at room temperature is of prime importance for the realization of scalable quantum networks. We perform Hong-Ou-Mandel (HOM) interference between photonic polarization states and single-photon-level pulses stored and retrieved from two sets of independent room-temperature quantum memories. We show that the storage and retrieval of polarization states from quantum memories does not degrade the HOM visibility for few-photon-level polarization states in a dual-rail configuration. For single-photon-level pulses, we measure the HOM visibility with various levels of background in a single polarization, single-rail QM, and investigate its dependence on the signal-to-background ratio. We obtain an HOM visibility of 43%, compared to the 48% no-memory limit of our set-up. These results allow us to estimate a 33% visibility for polarization qubits under the same conditions. These demonstrations lay the groundwork for future applications using large-scale memory-assisted quantum networks.

npj Quantum Information (2024)10:10 ; https://doi.org/10.1038/s41534-024-00803-2

INTRODUCTION

Quantum technologies have the promise of achieving several advantages in the fields of computation, metrology, and security[1]. The development of a large-scale quantum internet[2] is an encouraging route to attain quantum advantage using distributed quantum systems. To this end, elementary quantum networks have already been deployed, capable of distributing entanglement over tens to hundreds of kilometers[3–5]. However, developing more robust and accessible long-distance entanglement distribution networks brings the challenge of mitigating losses. To sidestep the inherent non-amplifiability of quantum signals, one can harness entanglement swapping[6], the basis of two-way quantum repeaters (QRs)[7], thereby extending the range over which quantum information can be distributed. Quantum memories (QMs)[8], when heralded, will play a crucial role in these repeaters[9], serving as temporary storage units coordinating qubit arrival at Bell-state measurement stations, significantly increasing the probability of successful entanglement swapping. While many types of QMs exist, room-temperature atomic ensembles provide a particularly appealing platform to develop scalable photonic quantum repeaters[10,11], the backbone for a user-defined entanglement-based quantum internet.

Currently, there are two types of quantum repeater network implementations with a degree of maturity. Type I is based upon the DLCZ protocol[7], wherein entanglement is generated by the interference of photons generated in quantum registers. While this method heralds the creation of entanglement between two registers, it has an inherently low rate[12]. Whereas in type II repeaters, entanglement is generated independent of the registers, and photons from separate entangled pairs are stored in a minimum of four in-out QMs after propagation[13]. Once there, their presence is heralded[14] and the intermediary photon's entanglement is swapped via a Bell-state measurement (BSM). By interfacing fast entanglement sources and fast quantum memories, rates can become several orders of magnitude higher than type I[15]. Recent studies have demonstrated this potential of integrating high-duty-cycle room-temperature atomic quantum memories with fast entanglement sources[10,16–19].

In the context of a type II repeater[20], for the swapping of entanglement to be successful, retrieved qubits from the in-out memories must maintain the same quantum state as their inputs, such as polarization[21–23] or time bin. The retrieved qubits must remain nearly indistinguishable from each other across all other crucial degrees of freedom, such as temporal and spectral profiles, thus the memories' performance must also remain nearly identical across those degrees of freedom as well as have similar overall efficiencies. A Hong-Ou-Mandel (HOM) interference measurement[24] on stored and released qubits[25] provides a method to verify this identical behavior of memories. Despite previous work focusing on type I[26,27] quantum repeaters, an experimental demonstration of HOM interference between two pulses of light retrieved from type II absorptive quantum memory systems—a significant stride toward demonstrating type II memory assisted entanglement swapping—remains to be shown.

Here, we demonstrate HOM interference between few-photon-level polarization states as well as single-photon-level pulses with a fixed polarization that have been stored and retrieved from independent type II absorptive quantum memory systems in dual and single-rail configurations respectively. In addition to this, we demonstrate this foundational measurement across four QMs, pairwise, in a configuration akin to a type II QR. We show that, in the limit of high signal-to-background ratio (SBR), the storage and retrieval of diagonal polarization states in our[21] warm Rb vapor quantum memories does not significantly degrade HOM visibility. We also show the detrimental effects of the background generated during the retrieval of single-photon-level pulses and

[1]Department of Physics and Astronomy, Stony Brook University, Stony Brook, NY 11794, USA. [2]Qunnect Inc., 141 Flushing Av. Suite 1110, Brooklyn, NY 11205, USA. [3]Department of Information Engineering, University of Padova, Via Gradenigo 6b, 35131 Padova, Italy. [4]Brookhaven National Laboratory, Upton, NY 11973, USA. [5]These authors contributed equally: Sonali Gera, Chase Wallace. ✉email: eden.figueroa@stonybrook.edu

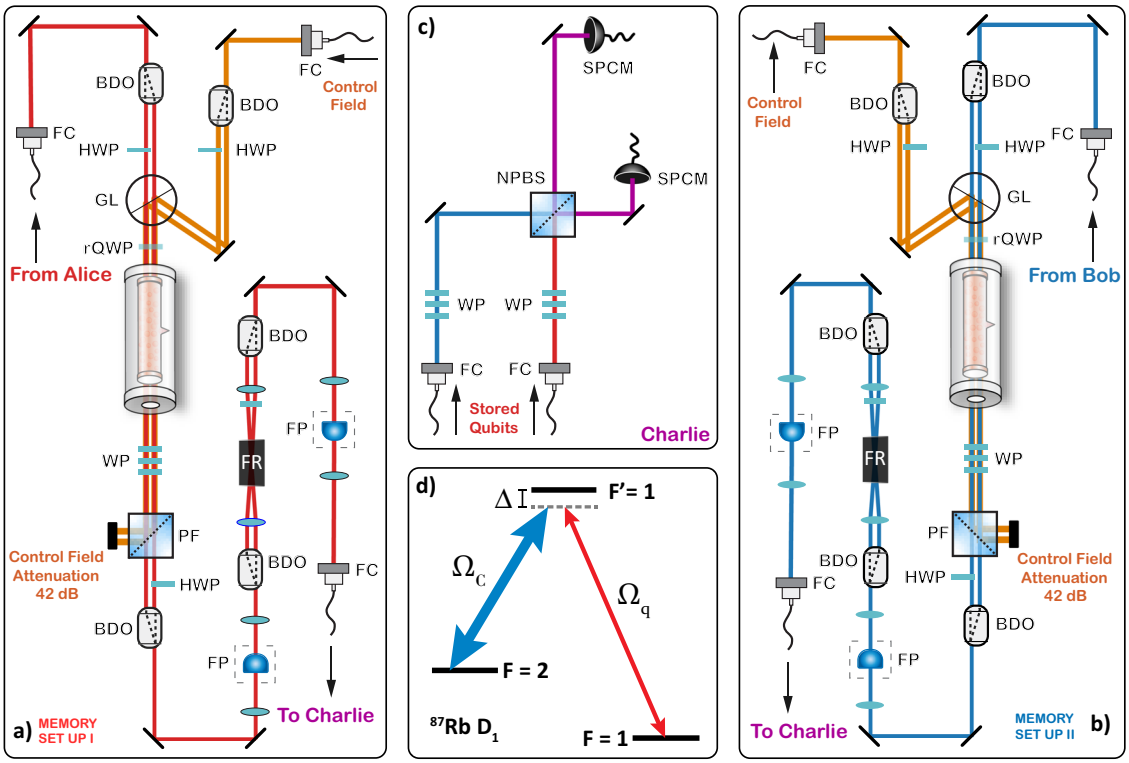

Fig. 1 QM HOM Interference set-up: four quantum light-matter interfaces forming two independent quantum memories for polarization states. a, **b** Quantum memory setups. After fiber propagation, the pulses are stored in two independent dual-rail atomic vapor quantum memories, consisting of the light-matter interfaces, and polarization and frequency filtering stages; **c** the outputs of the quantum memories are made to interfere at a 50:50 non-polarizing beamsplitter; **d** atomic level scheme for EIT storage in the ^{87}Rb D_1 line. Ω_C represents the strong control field, and Ω_q represents our weak probe/input pulse. They are red detuned from the $F' = 1$ transition by $\Delta = 400$ MHz. FC Fiber Collimator, BDO Beam Displacment Optics, HWP Half Wave Plate, WP Waveplate Combination, rQWP removable Quarter Wave Plate, GL Glan Laser Polarizer, PF Polarization Filtering, FP Fabry Perot Etalon, FR Faraday Rotator, NPBS Non Polarizing Beam Splitter, SPCM Single Photon Counting Modules.

describe a model quantifying the effect of this background on the HOM visibility. We also present a road map toward demonstrating even higher visibilities in HOM interference experiments using room-temperature quantum memories, laying the groundwork for memory-assisted BSMs of qubits and the first instance of a type II quantum repeater.

We present three sets of experiments, each highlighting a different aspect of memory performance. First, in section *Gen I QM HOM interference with few-photon-level polarization states*, we investigate the phase stability between the two rails and compatibility of our memories by storing few-photon-level diagonal polarization states in two independent room temperature quantum memories (Gen I[21]). We find no significant change in HOM visibility, compared to the case when no memories are involved, implying that the memories have high phase stability for the interference of polarization qubits and are compatible with one another. Second, in section *Gen I QM HOM interference at single-photon-level*, we investigate the single photon level operation of our memories and the potential detrimental effect of noise on HOM visibility in the same memory systems. Due to the high phase stability demonstrated previously, we switch to single-rail operation to focus on the single-photon level performance of our QMs. A decrease in HOM visibility is found and is attributed to a lower SBR due to a higher contribution from the memory background that exhibits no HOM interference. Third, in section *Gen II QM HOM interference at single-photon-level*, to thoroughly investigate this decrease in HOM visibility, noise reduction techniques are employed resulting in a second set of quantum memories (Gen II[23]) that provide an approximate five-fold increase in the SBR. Additionally, we present a model quantifying the dependence of HOM visibility on SBR. The model is experimentally verified by varying the region of interest for coincidence counting, effectively varying the SBR.

RESULTS

Gen I QM HOM interference with few-photon-level polarization states

Two independent sources of polarization states, herein called Alice and Bob, serve as inputs to two independent room-temperature quantum memories. The memories rely on electromagnetically induced transparency (EIT) in a lambda scheme to store and retrieve polarization states in the D_1 line of warm ^{87}Rb vapor, as shown in Fig. 1d. This is adapted in a dual rail configuration to store polarization states with high fidelity[21,28] (Fig. 1a, b). For our first set of experiments, we use two first-generation QMs to store and retrieve 400ns wide pulses. After retrieval, the pulses are made to interfere on a 50:50 beamsplitter, shown in Fig. 1c.

Histograms in Fig. 2a, b show the storage of two $|D\rangle$ polarized pulses from Alice and Bob in two dual-rail memories with a storage time of 1 μs, where the left and right rails store the $|V\rangle$ and $|H\rangle$ components of the pulses individually. The mean number of photons per pulse at the input of each memory is ~14 and ~10 for Alice and Bob respectively. In the absence of the atomic ensemble, the transmission through each memory setup is measured to be ~3% due to the low transmissions through each filtering etalon (35%), the Faraday isolator (50%), and various losses due to imperfect optics (50%). Owing to slightly different storage and fiber coupling efficiencies, we measure average photon numbers per stored pulse of ~ 0.024 and ~ 0.017 within a temporal region

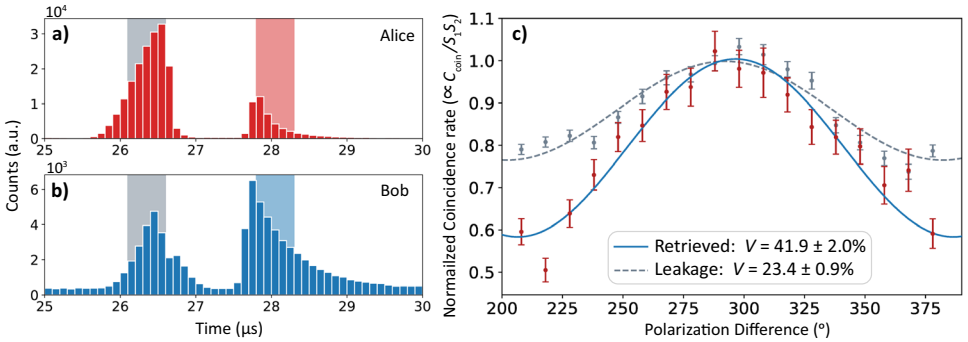

Fig. 2 HOM interference of polarization states retrieved from two Gen I quantum memories with few photon level inputs. a Histograms of single-photon detection events showing the temporal profile of the stored states in Alice's memory. The gray shaded region indicates the non-stored part of the pulse and the red shaded region indicates the part of the pulse that was stored and retrieved which contains about 0.024 photons per pulse. **b** For Bob's memory, the gray and blue shaded regions indicate the leakage and stored regions of interest respectively. The stored part contains about 0.017 photons per pulse. **c** The two detector coincidence rate is measured by varying the relative polarization of the retrieved pulses. We show the normalized coincidences after HOM interference for pulses that were stored and then retrieved from the memories (blue, $V = (41.9 \pm 2.0)\%$) and non-stored "leakage" photons (gray, $V = (23.4 \pm 0.9)\%$). Error bars represent the standard error of the mean.

of interest (ROI) marked by the red and blue shaded regions in Fig. 2a, b, from Alice and Bob's memory respectively. This ROI is post-selected with a width of 0.5μs beginning at the retrieval time, following the procedure outlined in[29].

By varying the polarization of one pulse with respect to the other at the HOM interference node we observe the desired modulation in the coincidence rate, exhibiting a minimum for the initial identical polarizations and reaching a maximum corresponding to orthogonal polarizations. The coincidences within the retrieval ROI, defined previously, are shown in red and fit to $\sim \cos^2$ curve, shown in blue in Fig. 2c. The interference visibility is measured to be $V = (41.9 \pm 2.0)\%$ for the retrieved states, which is consistent with the measured visibility of $(42.1 \pm 0.2)\%$ without the memories (see Methods section). For the case of HOM interference without memories, we attribute the low visibility to polarization drifts in the long non-polarization maintaining fibers used. Thus, we conclude that our memories have good phase stability and do not significantly affect the indistinguishability of the retrieved states.

The analysis detailed above is repeated with the two leftover "leakage" peaks, parts of the original input pulses that the memories do not store (gray shaded areas in Fig. 2a, b). Here, a lower HOM visibility of $V = (23.4 \pm 0.9)\%$ is measured due to a mismatch in their temporal envelopes as well as photon numbers (data shown in gray with the dashed gray curve as the fit in Fig. 2c).

Gen I QM HOM interference at single-photon-level

To more thoroughly investigate the effect of background we reduce the input mean photon number to contain on average ~1.6 photons per pulse. In addition, to eliminate any potential adverse effect due to imperfect polarization fidelity, we use the single-rail configuration of our memories (see Methods). In this single photon level regime, we measure signal-to-background ratio (SBR) of about 2.6, thus the contribution of coincidences from background photons becomes significant. Single photon level storage efficiencies of ~7% and ~18% are measured for Alice's and Bob's memories respectively, within the shaded red and blue temporal ROIs in Fig. 3a, b. To account for this imbalance, the fiber coupling efficiencies are adjusted such that the mean photon numbers of the retrieved photons at the two inputs of the beamsplitter are matched.

Input pulses are chosen to be 400ns wide and the storage times for both the memories are the same ($\tau_{Alice} = \tau_{Bob} = 0.9\mu s$), however their arrival times, and consequently their retrieval times, are changed. The difference in retrieval times serves as the temporal delay for the HOM interference (Fig. 3c). For each delay, in order to isolate the retrieved signal from the background, we looked for coincidences in the two detectors in the temporal region of interest (ROI) covering two 0.3μs regions in the retrieved pulses. Plotting the normalized coincidence rate versus the time delay, an HOM visibility of $(25.9 \pm 2.5)\%$ is obtained (Fig. 3d), where the maximum obtainable visibility is measured to be $(42.4 \pm 0.6)\%$ (see Methods section).

Comparing results from sections *Gen I QM HOM interference with few-photon-level polarization states* and *Gen I QM HOM interference at single-photon-level*, we find that lowering the mean number of photons in the input lowers the SBR and subsequently lowers the visibility. To explore this effect, the experiment is repeated without the input probe pulses, yielding only the background stemming from the strong control. As shown in gray dots in Fig. 3d, an HOM visibility that is consistent with zero is found; demonstrating the noise sources do not exhibit second-degree interference.

Gen II QM HOM interference at single-photon-level

In our next set of experiments, noise reduction techniques including an amplified spontaneous emission (ASE) filter for the control field, $\sigma^{\pm}$ polarization for the probe and control fields, new Fabry-Pérot etalons, along with several other improvements resulted in our second-generation quantum memories, jointly developed with Qunnect Inc.[23] based on a Stony Brook University patent[30]. These changes result in a lower background, yielding an SBR ranging from 1.7 to 11.9 depending on the size of the region of interest chosen, accompanied by an improved overall transmission of ~20%.

Gaussian pulses with a FWHM of 300ns and a mean photon number per pulse of ~1.6 serve as the inputs to the memories in a single-rail configuration (see Methods). After storage and retrieval from each memory, we measure the mean signal photon number to be ~0.01 at the inputs of the beamsplitter, excluding the background photons for the entirety of the retrieved pulse.

In this experiment, we utilize the full potential of our quantum memories by taking advantage of the arbitrary storage time feature. Here, pulses created by Alice and Bob reach the memories at the same time and the HOM interference is observed by varying the difference in storage times of the memories, $\Delta\tau \equiv \tau_{Alice} - \tau_{Bob}$. The storage times are varied by equal and opposite amounts ($\Delta\tau/2$), with the sum of Alice's and Bob's storage times staying constant at 4μs (Fig. 4a). For each run, $\Delta\tau$ is changed 25 times, and each time it is assigned a value at random from a predefined array in the range

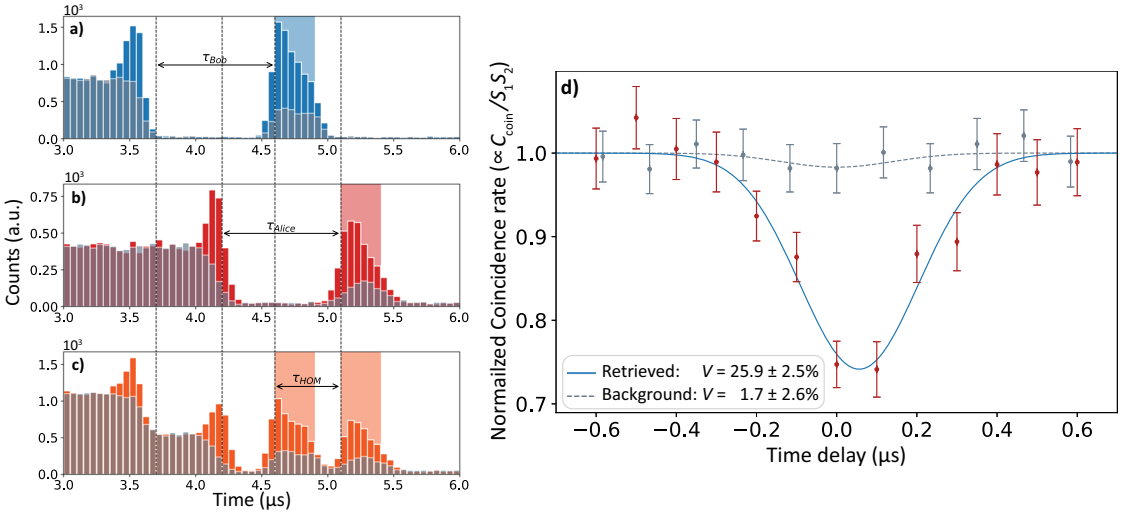

Fig. 3 HOM interference of pulses retrieved from two quantum memories with single-photon level inputs. a Histograms of single-photon detection events for the storage of light in Bob's memory containing 1.6 photons per pulse at the input; **b** same as (**a**) but for the storage of light in Alice's memory containing 1.6 photons per pulse at the input. **c** Counts in the single photon counters when both Alice and Bob pulses are sent together. The storage times are equal, $\tau_{Alice} = \tau_{Bob} = 0.9\mu s$. The time delay between retrieved pulses is indicated as τ_{HOM}. The lightly shaded histograms in (**a** - **c**) show the received counts without the input probe pulses and only the control field pulses, indicating the amount of background noise. The vertical shaded areas indicate the region of interest. **d** The normalized coincidence rate of retrieved pulses from memories at the measurement station (red points and blue fit). We obtain an interference visibility of $V = 25.9 \pm 2.5\%$. The coincidence rate for background photons is also shown, not exhibiting the HOM dip (gray dots and line). Error bars represent the standard error of the mean.

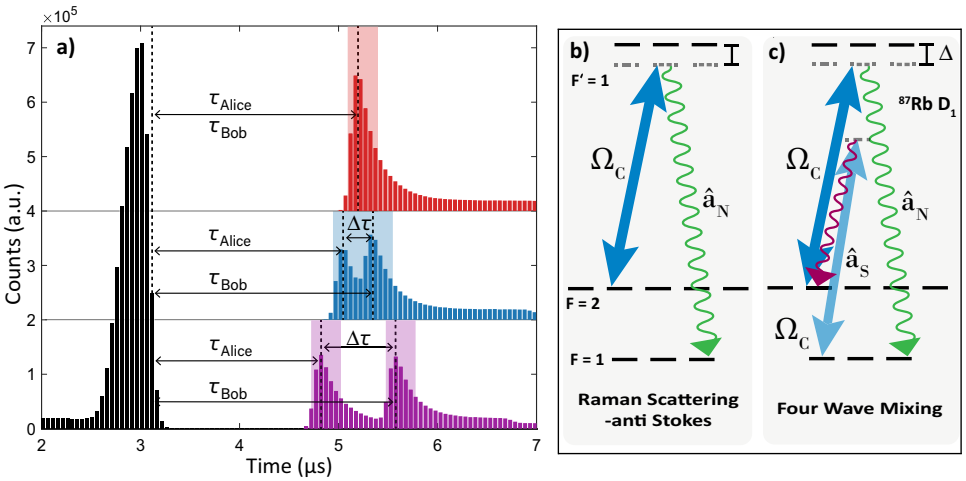

Fig. 4 Varying storage times for HOM interference with high SBR quantum memories with single photon level inputs. a Histograms of single-photon detection events from pulses, containing 1.6 photons per pulse, stored in two independent room temperature quantum memories. The difference in storage times, Δτ, is used as the delay for HOM interference. (black: histogram of events showing a portion of the unstored pulse, red: histogram of simultaneous storage in Alice and Bob memories, each with a storage time of $\tau = 2.0\mu s$, blue: histogram of storage events with a difference in storage times of $\Delta\tau = 0.3\mu s$, purple: difference in storage times $\Delta\tau = 0.75\mu s$). Shaded areas indicate an example of one region of interest used. **b** The atomic levels and fields relevant for noise induced by Spontaneous Raman Scattering (SRS). SRS occurring due to the resonant control, shown in dark blue, results in an anti-Stoke's field, $\hat{a}_N$, (green) at the same frequency as the signal, contributing to background noise. **c** The atomic levels and fields relevant for noise induced by Four Wave Mixing (FWM). The first step of FWM is the off-resonant coupling of the control, shown in light blue to the probe's transition, creating a Stokes field, $\hat{a}_S$, shown in purple, followed by the resonant control field creating an anti-Stokes field, $\hat{a}_N$ shown in green, at the same frequency and polarization as the signal. Compared to our first-generation quantum memories where the probe and control are linearly polarised, fewer channels are available for FWM and SRS to occur due to circularly polarized probe and control, reducing the amount of background in our second-generation quantum memories.

of -1.5 μs to 1.5 μs. Data is collected for 14 such runs for a total measurement time of 9 h.

For every Δτ, coincidences between the two detectors within specific temporal ROIs are analyzed with a wide coincidence window to cover the entirety of the retrieved pulse. By changing the size of ROI, we significantly change the signal count rate that gets included, while keeping the background count rate relatively constant, hence changing the SBR. Analyzing different regions of interest we find a maximum SBR of ~11.9, with a ROI of 160ns. Using the data within this ROI, the normalized coincidence rate versus Δτ is plotted in Fig. 5a; purple upward triangle. We measure an HOM visibility of $V = (42.9 \pm 3.4)\%$ with a new reference of $V = (48.5 \pm 0.5)\%$ measured without the memories (see Methods section). As before, the coincidence rate

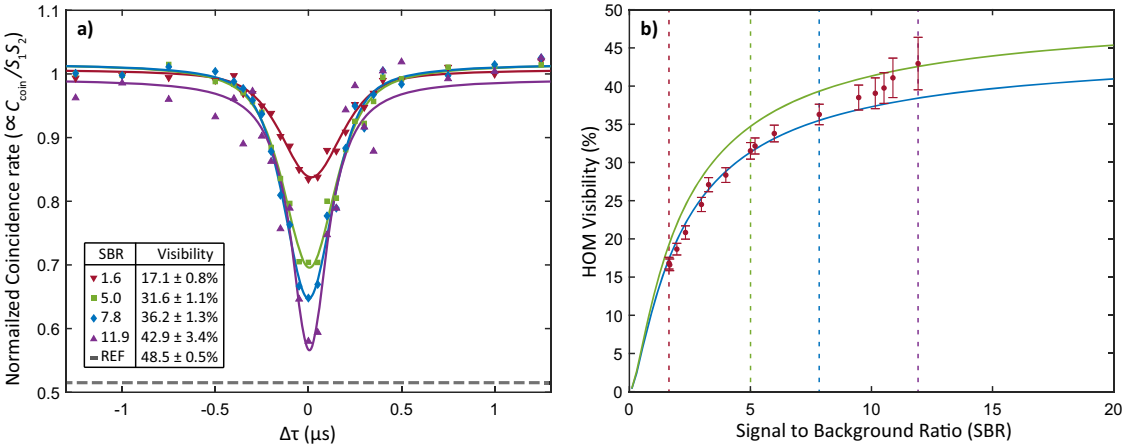

Fig. 5 Dependence of HOM visibility on the signal-to-background ratio. a HOM interference plotted for different estimated SBRs. Plots shown in red, green, blue, and purple show the HOM interference between photons that have been retrieved from the memories. These have visibilities of 17.1 ± 0.8%, 31.6 ± 1.1%, 36.2 ± 1.3%, and 42.9 ± 3.4% respectively. The black dashed line marks the measured visibility of 48.5 ± 0.5% between pulses when no memories were involved. As the estimated SBR increases from 1.6 in the red plot to 11.9 for the purple plot, the HOM dip gets closer to the limiting case of no memories shown as the black dashed line. Error bars are not shown for clarity but can be found in Supplementary Fig. 3. **b** Measured HOM visibility, red dots, versus the SBR. All data points were analyzed from the same data set. Each SBR reported is estimated from the number of counts within the regions of interest used and a region of the same size of only background counts. The blue curve is obtained by a fit to Eq. (1) where V_0 is the fit parameter, and reaches 45.5% in the limit of infinite SBR. The green curve shows the ideal case of $V_0 = 0.5$. The dotted red, green, blue, and purple lines mark the SBRs plotted in (**a**) respectively. Error bars represent the standard error of the mean.

between the background noise photons exhibited no HOM interference.

To evaluate the significance of such an increase in visibility, a quantitative analysis of the effect of a non-interfering field on the HOM visibility is presented. In this model, additional coincidences occur due to background-signal and background-background detections. Factoring in these erroneous coincidences, one obtains a simple expression demonstrating these detrimental effects (see Supplementary Notes):

$$V = V_0\left(\frac{R}{1+R}\right)^2, \tag{1}$$

where R is the SBR, and V_0 is the HOM visibility with no background. To show this dependence of HOM visibility on SBR, the above data analysis is repeated on the same data set for several ROIs, each resulting in a different estimated SBR (Fig. 5b). A fit to the model (Eq. (1)) indicates that the maximum achievable visibility is 45.5%, differing from the 48.5% measured without the memories. We believe this is primarily due to a slight mismatch in memory efficiencies, variations in mean photon number, and slow drifts in polarization in the memory output fibers. Additionally, this model indicates we are nearing the plateau of visibility using quantum memories.

DISCUSSION

Our work shows that warm-atomic-vapor quantum memories that have high SBR at single-photon levels, as demonstrated here, will be a viable option for applications in memory-assisted operations that require a high degree of indistinguishability. Some examples of such operations include entanglement swapping operations for continuous variable qubits using single-rail QMs[31,32]; as well as quantum gates[33], memory-assisted BSMs, memory-assisted measurement-device-independent quantum-key-distribution (MA-MDI-QKD), and entanglement swapping operations for polarization qubits[9] realized in a dual-rail configuration[34]. Our results are summarized in Table 1 and highlight different aspects of our QM performance. The first measurement demonstrated that storing and retrieving high SBR polarization states from a warm atomic vapor appears to have a minimal effect on the visibility of HOM interference. Further, we showed that a dual-rail configuration does not compromise HOM visibility due to its high polarization fidelity, pointing to the reliability of the dual-rail setup. Results from our second set of measurements confirm that the background associated with this storage technique exhibits no HOM interference, significantly reducing visibility during low signal-to-background ratio (SBR) retrieval conditions. Finally, our third set of measurements demonstrated that the visibility for single-rail operations is appreciably enhanced by implementing known techniques for background reduction. This allowed us to

Table 1. Measured HOM visibilities for Gen I and II experiments.

Config.	⟨n⟩	DOF	ROI(μs)	V_{HOM}	SBR
No memories	0.4	Pol	N/A	(42.1 ± 0.2)%*	$\mathcal{O}(10^3)$
	0.4	Delay	N/A	(42.4 ± 0.6)%*	$\mathcal{O}(10^3)$
	0.5	Delay	N/A	(48.5 ± 0.5)%†	$\mathcal{O}(10^3)$
Gen I Dual-rail	13	Pol	1.00	(35.8 ± 1.7)%*	24
	13		0.50	(41.9 ± 2.0)%*	37
Gen I Single-rail	1.6	Delay	1.30	(20.3 ± 2.3)%*	2.4
	1.6		0.60	(25.9 ± 2.5)%*	2.6
Gen II Single-rail	1.6	Storage Time	1.28	(31.6 ± 1.1)%†	5.0
	1.6		0.64	(36.2 ± 1.3)%†	7.8
	1.6		0.16	(42.9 ± 3.4)%†	11.9

*Using the measurement station for the Gen I memories

†Using the measurement station for the Gen II memories

Different experimental configurations adopted (without memories, with dual rail memory operation, and with single rail memory operation). ⟨**n**⟩ is the mean photon number at the input of the memories or BS(in case of no memory operation), *DOF* is the degree of freedom that is scanned to obtain the HOM dip. Here, *Pol* is the polarization of Alice's pulse wrt Bob's, Delay: time of arrival of Alice's pulse wrt Bob's, *Storage Time is difference in* the storage time of Alice wrt to Bob's. *ROI* is the width of the region of interest (ROI) time window to record coincidences, V_{HOM} is the measured visibility and *SBR* is the estimated signal-to-background ratio.

establish a quantifiable relationship between HOM visibility and SBR. With this relationship, depicted in Fig. 5, the results of section *HOM interference with few-photon-level polarization states*, and an anticipated 50% reduction in the SBR on switching to dual-rail configuration[21,23], we predict that our current gen II systems would achieve an HOM visibility of about 33% for dual-rail operation with polarization qubits.

From these predictions, our QMs would be useful in the context of entanglement swapping under ideal conditions in their current state. In an entanglement swapping experiment with a $|\Psi^-\rangle$ Bell state projection using only a beam splitter, the probability of a successful swap is given by the HOM visibility[35,36]. Using the Peres-Horodecki criterion, assuming perfect efficiencies and 100% initial entanglement fidelities, we can see that the swapped states will be entangled if $V_{\mathrm{HOM}} > 1/3$ and will violate the CHSH inequality if $V_{\mathrm{HOM}} > 1/\sqrt{2} \approx 71\%$ for single-photon Fock states[37,38]. Assuming 100% heralding efficiencies, which results in single-photons having the same fidelities as coherent states in the memories[39], we would expect an HOM visibility of 66% for the current level of noise, far surpassing the 33% limit for entanglement and nearing the 71% CHSH bound.

To surpass these bounds, several hurdles still exist toward using warm atomic vapor QMs in memory-assisted measurements and operations. As evidenced in this study, mitigating the noise associated with these memories stands as a paramount challenge to achieve indistinguishable retrieved qubits. While background reduction techniques have been deployed in our systems, further improvements can be achieved by utilizing cavity mode selection, optical pumping, and active manipulation of the EIT Hamiltonian. Furthermore, it is possible to increase the concentration of the signal with respect to the background by using a shorter signal pulse on the condition of no adverse effect on efficiency[40]. Short pulses also have the added benefit of more closely mimicking the temporal profile of photons retrieved from cavity-enhanced SPDC entanglement sources such as the ones we deploy in our laboratory. We predict that narrowing pulse widths by a factor of 10, i.e. 300ns → 30ns, will likely result in an order of magnitude increase in the SBR reaching ~120 in a single-rail configuration. In conjunction with the use of a superconducting nanowire detector to effectively decrease our dark counts rates to near zero, we believe we will be able to achieve an HOM visibility of nearly 50% with our second-generation QMs.

Moreover, to be used in a scaleable manner in large quantum communication systems, these memory systems must display seamless compatibility with single-photon and entanglement sources. We have implemented and demonstrated the interoperability of four room-temperature atomic quantum memories, the minimum number of memories required for a type II quantum repeater. We envision using our second-generation QMs to facilitate entanglement swapping at the central node, while in parallel, upgraded first-generation QMs will buffer the external nodes. To implement the basic framework of a first-generation quantum repeater, high SBR storage of single-photons from a bright entanglement source will be crucial. Recent developments have demonstrated the storage of single photons originating from SPDC sources[18]. Additionally, there have been successful interactions between single photons emitted by quantum dot sources and room-temperature atomic quantum memories[19,41]. These cutting-edge techniques for photon pair generation represent the most promising contenders for a high repetition source of entangled photons with linewidths compatible with our atomic quantum memories.

Additionally, these memories must have single-photon heralding capabilities, without which a QM would only be providing loss to the system. Given the current advances in memory-source interactions with high repetition rate sources, heralding these interactions in real-time is the only major scientific milestone that needs to be met in order to realize a practical type II quantum repeater network. This milestone stands as the core focus of our forthcoming experiments which will build upon our previous work[42], wherein we successfully detect the presence of a signal field in an atomic memory through a non-demolition measurement that employs quantum state tomography to measure the change in the phase of a probe field that co-propagates with the signal. We envision adopting this phase-phase photon-photon non-linear system to herald the presence of a single photon in our quantum memories in real-time.

Lastly, we anticipate that one of the several immediate applications of our type II repeater network topology could be buffering streams of random polarization qubits to be employed in a variable-delay MDI-QKD protocol[43,44] and Bell-state measurements. The memory-assisted protocols require that Alice and Bob create qubits and send them through their respective channels where they are stored in their respective memories. Once both memories are loaded and heralded, they are simultaneously read, and the rest of the protocol is identical to standard MDI-QKD. We have adopted the approach from[45] to predict the secret key rate for a possible implementation of MA-MDI-QKD protocol using our network (see Supplementary Discussion). The model predicts that with our current Gen II memory parameters and an achievable signal to background of 135, it is possible to achieve a positive key rate.

METHODS

Quantum memories

All our memories rely on electromagnetically induced transparency (EIT) to store and retrieve pulses in the D_1 line of a warm ^{87}Rb vapor. As shown in Fig. 1d, we use a lambda system with a red single photon detuning of 400 MHz for both probe and control fields. The control field is tuned to the $F = 2 \leftrightarrow F' = 1$ transition, to create a window of transparency for our orthogonally polarized probe tuned to the $F = 1 \leftrightarrow F' = 1$ transition.

Storage of polarization states is achieved in a dual-rail configuration, where beam displacement optics (BDO) placed at the input of the memory map an arbitrary superposition of $|H\rangle$ and $|V\rangle$ polarization modes onto a spatial superposition of the left and right rails. These BDOs consist of Calcite beam displacers for our first-generation QMs and utilize a Sagnac interferometer-like configuration to separate the rails in our second-generation QMs. The two rails of the control beam coherently prepare two volumes in the ^{87}Rb vapor cell, enabling storage in both rails. The stored polarization states can be retrieved on-demand by changing the timing of the "read" control pulse. For the single-photon-level experiments performed in this paper, the memories are arranged in a single-rail configuration. This is done simply by aligning the input polarization with one of the input rails and blocking the opposing rails' probe and control fields.

After storage, polarization filtering is used to attenuate the majority of the strong control field. Afterward, the rails are recombined, restoring the input polarization, and frequency filtering etalons are utilized to further attenuate the control field[28], as seen in Fig. 1a, b. The relevant parameters of the quantum memories are calibrated to ensure that all four memory rails (required to store two independent polarization states) had near identical EIT bandwidths and storage efficiencies Fig. 6.

These warm vapor QM systems have three main sources of background all related to the control field employed to achieve the transparency window required for storage. In increasing order of significance, they are: the unfiltered control field, unfiltered amplified spontaneous emission (ASE) coming from the tapered amplified laser used for the control field, and background due to atomic effects such as four-wave-mixing (FWM) and spontaneous Raman scattering (SRS) that produce noise with similar frequency and polarization to that of the stored pulses (Fig. 4b, c).

While the vast majority of the control field is attenuated in the Gen I QMs, these sources of background persist at an appreciable

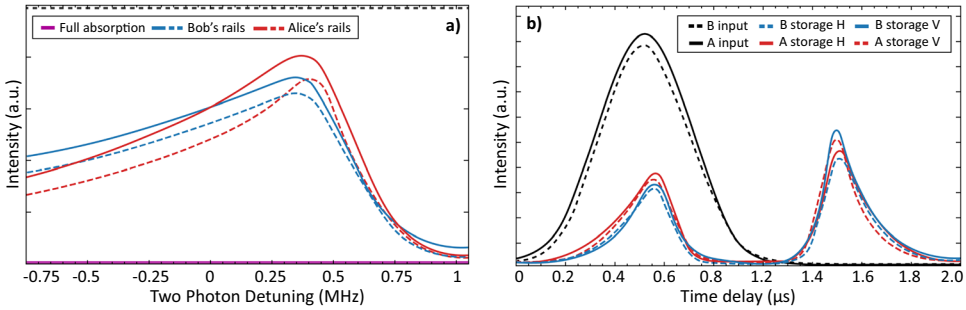

Fig. 6 Gen I dual-rail memory characterization. a Matched EIT lines for $|H\rangle$ and $|V\rangle$ rails in both light-matter interfaces. EIT resonances for each rail of Alice's and Bob's memory are in red and blue, respectively. The top dashed black line represents memory-free transmission, and the purple line at the bottom represents full atomic absorption. All EIT lines are matched to have a ~ 1MHz FWHM linewidth; **b** black curves show the temporal profiles of the input pulses created by Alice(continuous) and Bob(dashed). The red and blue curves show the classical storage of Alice's and Bob's pulses in their respective memories. Red dashed for $|V\rangle$ and continuous for $|H\rangle$ for Alice. Blue dashed for $|H\rangle$ and continuous for $|V\rangle$ for Bob. All four storage signals are matched with independent control fields to achieve ~20% storage efficiency at the classical level.

level. To reduce these background sources in the experiments with the Gen II QMs, a Volume Bragg Grating with a FWHM of 50GHz is employed to remove the background associated with ASE and new Fabry-Pérot etalons with a higher transmission for the probe field and higher suppression of the control are employed. In addition to these changes, the utilization of $\sigma^{\pm}$ polarization for the probe and control fields suppresses[46] the background from FWM and SRS. More details about the QMs presented in this manuscript can be found in the Supplementary Methods section and Supplementary Table 1.

Pulse generation

Two independent sources (Alice and Bob) create memory-compatible polarization states using attenuated coherent pulses from a laser. Both Alice and Bob's set-ups consist of acousto-optic modulators (AOMs) to temporally pulse the attenuated light to have a Gaussian envelope. Since the pulses are created from the same laser, we employ a phase modulator in one arm to randomize the phases of Alice's pulses with respect to Bob's. For all the measurements presented in this paper, the Gaussian pulses have a temporal FWHM ranging from 200-400ns, within the 1μs coherence time of our laser.

HOM measurement station calibration

To calibrate the measurement station for different polarization states, the light is routed directly to the measurement station, bypassing the memories. By varying the polarization state of Bob's pulse with respect to Alice's, the relative polarization between the signals is utilized to measure HOM interference. In this case, 400ns Gaussian pulses containing ~ 0.4 photons per pulse are used. Eventually, perpendicular polarizations result in two entirely distinguishable photons with a maximum coincidence rate at the outputs of the beamsplitter. The normalized coincidences are fitted to $cos^2(\phi)$, where ϕ is the relative polarization, see Supplementary Fig. 1. To ensure that the setup is balanced for all the input states, polarization HOM interference is observed for horizontal, vertical, diagonal, and anti-diagonal polarizations, showing on average a visibility of $(42.1 \pm 0.2)\%$. This measurement set-up is deployed for measurements presented in section *HOM interference with few-photon-level polarization states*.

To more closely mimic the delay experiments with the memories, the time delay, thus the temporal overlap of the pulses are scanned with the light once again routed around the memory. Both Alice and Bob create 200ns wide Gaussian pulses that are horizontally polarized and contain on average ~ 0.4 photons per pulse. The temporal overlap of the two wave functions is scanned by changing the timing of pulse generation between Alice and Bob. The rate of coincidence counts between the output ports of the beamsplitter is measured using a coincidence window of 1μs. We measure a visibility of $V = (42.4 \pm 0.6)\%$ from the fit at zero delay. As expected[47], the width of the HOM curve precisely matches the temporal width of the input pulses. For the experiments with the Gen II memories, presented in section *Gen II QM HOM interference at single-photon-level*, we use a new measurement station with a visibility of at least $V = (48.5 \pm 0.5)\%$, measured using a similar procedure as before. These measured visibility values serve as a reference for the HOM interference with single photon level pulses retrieved from the quantum memories.

For all delay experiments, with and without the memories, a series of wave plates are employed before the beam splitter in each arm to correct for any unitary transformations of the polarization during propagation through the fibers. This transformation is analyzed periodically, outside of measurement time, using a continuous wave reference through the setup and measured with a polarimeter.

DATA AVAILABILITY

The data that supports the findings of this study is available upon request.

CODE AVAILABILITY

The code that supports the findings of this study is available upon request.

Received: 13 February 2020; Accepted: 4 January 2024;
Published online: 15 January 2024

REFERENCES

1. Awschalom, D. et al. Development of quantum interconnects (quics) for next-generation information technologies. *PRX Quant.* **2**, 017002 (2021).
2. Wehner, S., Elkouss, D. & Hanson, R. Quantum internet: a vision for the road ahead. *Science* **362**, eaam9288 (2018).
3. Yu, Y. et al. Entanglement of two quantum memories via fibres over dozens of kilometres. *Nature* **578**, 240–245 (2020).
4. van Leent, T. et al. Entangling single atoms over 33 km telecom fibre. *Nature* **607**, 69–73 (2022).
5. Neumann, S. P., Buchner, A., Bulla, L., Bohmann, M. & Ursin, R. Continuous entanglement distribution over a transnational 248km fiber link. *Nat. Commun.* **13**, 453–467(2022).
6. Pan, J.-W., Bouwmeester, D., Weinfurter, H. & Zeilinger, A. Experimental entanglement swapping: entangling photons that never interacted. *Phys. Rev. Lett.* **80**, 3891 (1998).
7. Duan, L.-M., Lukin, M. D., Cirac, J. I. & Zoller, P. Long-distance quantum communication with atomic ensembles and linear optics. *Nature* **414**, 413–418 (2001).
8. Lvovsky, A. I., Sanders, B. C. & Tittel, W. Optical quantum memory. *Nat. Photon.* **3**, 706–714 (2009).

9. Azuma, K. et al. Quantum repeaters: from quantum networks to the quantum internet. *Rev. Modern Phys.* **95**, 045006 (2023).
10. Ma, L. et al. High-performance cavity-enhanced quantum memory with warm atomic cell. *Nat. Commun.* **13**, 2368 (2022).
11. Dideriksen, K. B., Schmieg, R., Zugenmaier, M. & Polzik, E. S. Room-temperature single-photon source with near-millisecond built-in memory. *Nat. Commun.* **12**, 3699 (2021).
12. Moehring, D. L. et al. Entanglement of single-atom quantum bits at a distance. *Nature* **449**, 68–71 (2007).
13. Lloyd, S., Shahriar, M., Shapiro, J. & Hemmer, P. Long distance, unconditional teleportation of atomic states via complete bell state measurements. *Phys. Rev. Lett.* **87**, 167903 (2001).
14. Bhaskar, M. K. et al. Experimental demonstration of memory-enhanced quantum communication. *Nature* **580**, 60–64 (2020).
15. Muralidharan, S. et al. Optimal architectures for long distance quantum communication. *Sci. Rep.* **6**, 20463 (2016).
16. Li, H. et al. Heralding quantum entanglement between two room-temperature atomic ensembles. *Optica* **8**, 925–929 (2021).
17. Thomas, S. et al. Deterministic storage and retrieval of telecom quantum dot photons interfaced with an atomic quantum memory. *arXiv* https://arXiv.org/abs/2303.04166 (2023).
18. Buser, G., Mottola, R., Cotting, B., Wolters, J. & Treutlein, P. Single-photon storage in a ground-state vapor cell quantum memory. *PRX Quant.* **3**, 020349 (2022).
19. Cui, G. D. et al. Coherent quantum interconnection between on-demand quantum dot single photons and a resonant atomic quantum memory. *arXiv* https://arXiv.org/abs/2301.10326 (2023).
20. Lago-Rivera, D., Grandi, S., Rakonjac, J. V., Seri, A. & de Riedmatten, H. Telecom-heralded entanglement between multimode solid-state quantum memories. *Nature* **594**, 37–40 (2021).
21. Namazi, M., Kupchak, C., Jordaan, B., Shahrokhshahi, R. & Figueroa, E. Ultralow-noise room-temperature quantum memory for polarization qubits. *Phys. Rev. Appl.* **8**, 034023 (2017).
22. Namazi, M. et al. Free-space quantum communication with a portable quantum memory. *Phys. Rev. Appl.* **8**, 064013 (2017).
23. Wang, Y., Craddock, A. N., Sekelsky, R., Flament, M. & Namazi, M. Field-deployable quantum memory for quantum networking. *Phys. Rev. Appl.* **18**, 044058 (2022).
24. Hong, C. K., Ou, Z. Y. & Mandel, L. Measurement of subpicosecond time intervals between two photons by interference. *Phys. Rev. Lett.* **59**, 2044–2046 (1987).
25. Jin, J. et al. Two-photon interference of weak coherent laser pulses recalled from separate solid-state quantum memories. *Nat. Commun.* **4**, 2386 (2013).
26. Stolk, A. et al. Telecom-band quantum interference of frequency-converted photons from remote detuned nv centers. *PRX Quant.* **3**, 020359 (2022).
27. Du, D. et al. An elementary 158 km long quantum network connecting room temperature quantum memories. *arXiv* https://arXiv.org/abs/2101.12742 (2021).
28. Kupchak, C. et al. Room-temperature single-photon level memory for polarization states. *Sci. Rep.* **5**, 7658 (2015).
29. Nölleke, C. et al. Efficient teleportation between remote single-atom quantum memories. *Phys. Rev. Lett.* **110**, 140403 (2013).
30. Figueroa, E., Namazi, M., & Flament, M. Devices, systems, and methods facilitating ambient-temperature quantum information buffering, storage, and communication. *US Patent* **11**, 218–228 (2022).
31. Dias, J., Winnel, M. S., Hosseinidehaj, N. & Ralph, T. C. Quantum repeater for continuous-variable entanglement distribution. *Phys. Rev. A* **102**, 052425 (2020).
32. Goncharov, R. et al. Quantum repeaters and teleportation via entangled phase-modulated multimode coherent states. *Phys. Rev. Appl.* **20**, 044030 (2023).
33. Stolz, T. et al. Quantum-logic gate between two optical photons with an average efficiency above 40%. *Phys. Rev. X* **12**, 021035 (2022).
34. Cao, M., Hoffet, F., Qiu, S., Sheremet, A. S. & Laurat, J. Efficient reversible entanglement transfer between light and quantum memories. *Optica* **7**, 1440–1444 (2020).
35. Zhang, Y. et al. Simultaneous entanglement swapping of multiple orbital angular momentum states of light. *Nat. Commun.* **8**, 632 (2017).
36. Samara, F. et al. Entanglement swapping between independent and asynchronous integrated photon-pair sources. *Quant. Sci. Technol.* **6**, 045024 (2021).
37. Peres, A. Separability criterion for density matrices. *Phys. Rev. Lett.* **77**, 1413 (1996).
38. Clauser, J. F., Horne, M. A., Shimony, A. & Holt, R. A. Proposed experiment to test local hidden-variable theories. *Phys. Rev. Lett.* **23**, 880 (1969).
39. Michelberger, P. et al. Interfacing ghz-bandwidth heralded single photons with a warm vapour raman memory. *J. Phys.* **17**, 043006 (2015).
40. Wolters, J. et al. Simple atomic quantum memory suitable for semiconductor quantum dot single photons. *Phys. Rev. Lett.* **119**, 060502 (2017).
41. Kroh, T. et al. Slow and fast single photons from a quantum dot interacting with the excited state hyperfine structure of the cesium d1-line. *Sci. Rep.* **9**, 13728 (2019).
42. Sagona-Stophel, S., Shahrokhshahi, R., Jordaan, B., Namazi, M. & Figueroa, E. Conditional π-phase shift of single-photon-level pulses at room temperature. *Phys. Rev. Lett.* **125**, 243601 (2020).
43. Kaneda, F., Xu, F., Chapman, J. & Kwiat, P. G. Quantum-memory-assisted multi-photon generation for efficient quantum information processing. *Optica* **4**, 1034–1037 (2017).
44. Xu, F., Qi, B., Liao, Z. & Lo, H. K. Long distance measurement-device-independent quantum key distribution with entangled photon sources. *Appl. Phys. Lett.* **103**, 87–106 (2013).
45. Panayi, C., Razavi, M., Ma, X. & Lütkenhaus, N. Memory-assisted measurement-device-independent quantum key distribution. *New J. Phys.* **16**, 043005 (2014).
46. Zhang, K. et al. Suppression of the four-wave-mixing background noise in a quantum memory retrieval process by channel blocking. *Phys. Rev. A* **90**, 033823 (2014).
47. Legero, T., Wilk, T., Hennrich, M., Rempe, G. & Kuhn, A. Quantum beat of two single photons. *Phys. Rev. Lett.* **93**, 070503 (2004).

ACKNOWLEDGEMENTS

We acknowledge M. Avesani and A. Stanco for assistance in developing the FPGA control used in the first-generation experiments as well as Dr. B. Jordaan and Dr. R. Shahrokhshahi for their assistance in the early stages of the experiment. We thank Dr. G. Cui and L. Castillo-Veneros for their assistance in automating the data acquisition of the second-generation experiments. We would also like to thank Dr. Y. Wang for helpful discussions. Additionally, we acknowledge L. Castillo-Veneros, Dr. J. Martínez-Rincón, Dr. P. Stankus and A. Del Valle for their assistance in proofreading and editing the manuscript. This work was supported by the U.S. Office of Naval Research grant 00141410801, the National Science Foundation grants PHY-1404398, the Simons Foundation grant SBF-241180 and the DOE ASCR grant: "Inter-campus network enabled by atomic quantum repeater nodes". M. F. and S. S. acknowledge financial assistance from the United States Department of Education through a GAANN Fellowship P200A150027-17. S.G. acknowledges support from the QISE-Net program, NSF award DMR-1747426. C.W. and E.F. acknowledge support from the Center for Distributed Quantum Processing at Stony Brook University.

AUTHOR CONTRIBUTIONS

S.G. and C.W. participated in setting up the experimental apparatus, data taking, data analysis, and preparing and editing the manuscript. Y.K., A.S., S.S., G.V. and P.V. participated in data taking and analysis for the first-generation QMs. M.F. and M.N. participated in the development of the second-generation QMs as well as editing the manuscript. E.F. conceptualized and supervised the experimental efforts.

COMPETING INTERESTS

M.F., M.N. and E.F. have shares of Qunnect Inc., a quantum technology company based in NY. All other authors declare no competing interests.

ADDITIONAL INFORMATION

Supplementary information The online version contains supplementary material available at https://doi.org/10.1038/s41534-024-00803-2.

Correspondence and requests for materials should be addressed to Eden Figueroa.

Reprints and permission information is available at http://www.nature.com/reprints

Publisher's note Springer Nature remains neutral with regard to jurisdictional claims in published maps and institutional affiliations.